The absolute effective area of the Chandra high resolution mirror assembly (HRMA)

D. A. Schwartz[a], L. P. David[a], R. H. Donnelly[a], R. J. Edgar[a], T. J. Gaetz[a], D. E. Graessle[a], D. Jerius[a], M. Juda[a], E. M. Kellogg[a], B. R. McNamara[a], P. P. Plucinsky[a], L. P. VanSpeybroeck[a], B. Wargelin[a], S. Wolk[a], P. Zhao[a], D. Dewey[b], H. L. Marshall[b], N. S. Schulz[b], R. Elsner[c], J. Kolodziejczak[c],S. L. O'Dell[c], D. A. Swartz[c] A. Tennant[c], and M. C. Weisskopf[c],

[a]Harvard-Smithsonian Center for Astrophysics, 60 Garden St., Cambridge MA, USA
[b]Massachusetts Institute of Technology, Cambridge MA, USA
[c]NASA/George C. Marshall Space Flight Center, Huntsville AL, USA

ABSTRACT

The Chandra X-ray Observatory was launched in July 1999, and is returning exquisite sub-arc second X-ray images of star groups, supernova remnants, galaxies, quasars, and clusters of galaxies. In addition to being the premier X-ray observatory in terms of angular and spectral resolution, Chandra is the best calibrated X-ray facility ever flown. We discuss here the calibration of the on-axis effective area of the High Resolution Mirror Assembly. Because we do not know the absolute X-ray flux density of any celestial source, this must be based primarily on ground measurements and on modeling. We use celestial sources which may be assumed to have smoothly varying spectra, such as the the BL Lac object Markarian 421, to verify the continuity of the area calibration as a function of energy across the Ir M-edges. We believe the accuracy of the HRMA area calibration is of order 2%.

Keywords: Chandra Observatory, X-ray astronomy, X-ray telescopes, Calibration

1. INTRODUCTION

The Chandra X-ray observatory has exceeded our expectations for the imaging capability[1,2] of the high resolution mirror assembly (HRMA). The convolution of the HRMA imaging, the focal plane science instruments, and the aspect solution reconstruction, (which are all comparable and therefore not yet completely separated), results in a point spread function with half power radius less than $0.5''$. This is a factor of 10 improvement in our linear ability to distinguish two point sources, and a factor of 100 increase in the available picture elements in an X-ray image!

This paper discusses the effective area of the mirror on-orbit. Briefly, the key relevant features are that the HRMA consists of four nested shells, of inner diameters from 0.6 to 1.2 m, and grazing angles for on-axis radiation of $27.1'$, $36.4'$, $41.3'$, and $51.3'$. The mirrors are composed of zerodur glass, coated with an ~ 95 Å chromium binding layer and ~ 325 Å iridium reflecting layer.

The effective area of a mirror is a fundamental concept which allows us to convert an observed counting rate into quantities of physical interest. In an idealized situation of a perfect detector, an observed counting rate R(E) of photons of energy E allows us to deduce an incident photon flux of $F = R(E)/A(E)$ photons cm^{-2} s^{-1}, where A(E) is the effective area of the mirror at energy E. More generally

$$R_i(E') = \int Q_i(E, E')\, A(E, \theta, \phi)\, F(E) dE, \tag{1}$$

where $A(E, \theta, \phi)$ is the effective area to photons of energy E at an off-axis angle (θ, ϕ), $Q_i(E, E')$ is the quantum efficiency of the detector times the redistribution function for a photon of incident energy E to appear as if it has energy E' for an event selected according to a set of criteria `{i}`, F(E) is the spectral flux of the source being observed, and $R_i(E')$ is the observed counting rates of events satisfying criteria `{i}` and appearing to have energy E'. In an astronomical observation we typically formulate a hypothesis of the function F(E) involving free parameters, and adjust those parameters until the predicted counting rates $R_i(E')$ in Eq. (1) match the data sufficiently well.

This paper deals only with the effective mirror area, and more specifically only with the on axis effective area $A(E) \equiv A(E, \theta = 0, \phi$ indeterminate). The general effective area can be expressed $A(E, \theta, \phi) = A(E) \times V(E, \theta, \phi)$,

where the dimensionless vignetting function has values $1 \geq V \geq 0$. Studying A(E) by itself is useful, and indeed necessary, despite the fact that ultimately it is only the product $A \times Q$ which is needed for the scientific analysis. This is because one wants to break down the response functions into their simplest, physical constituents, and because the mirror portion of the response, A, remains constant while we make observations with different instruments, having different responses Q_i.

Even if Q were extremely well known, which is feasible but not yet realized, it would be impossible to use Eq. (1) to determine A because F(E) is not known (to the desired accuracy) for any celestial X-ray source. We expect that part of the legacy of the Chandra Observatory will be to establish flux standards on the sky, and to cross calibrate other contemporaneous X-ray missions.

Instead, a large number of steps go into the derivation of the HRMA effective area on-orbit. We performed extensive ground measurements on the flight HRMA, at the NASA/MSFC X-ray calibration facility (XRCF). We performed synchrotron measurements of the effective optical constants of the Ir surfaces. We combined the above measurements, and the optical metrology of the HRMA element figuring and alignment, into a raytrace model. Predictions of this model were compared to the XRCF measurements, discrepancies were investigated, and some modifications were implemented. Small residual discrepancies remained. We fit these to an *ad hoc* polynomial correction factor. We then used our raytrace model to predict the effective area on-orbit, including the same polynomial correction factor.

Several significant improvements have been made in the analysis since our previous reports.[3–5] These include self-consistent methods of treating surface roughness when deriving and when using the Ir optical constants, improved knowledge of the response function of the solid state detectors used in the XRCF measurements, use of optical constants derived from our synchrotron measurements throughout the range 0.94 to 10 keV, and an improved derivation of optical constants by accounting for a layer of contamination on our witness flats. This allows us to predict the total HRMA area measured at XRCF to within 4%.

2. XRCF MEASUREMENTS

An extensive calibration program was carried out on the flight HRMA at the MSFC/XRCF. Figure 1 shows the configuration for these measurements. An X-ray source system (XSS) capable of generating principal X-ray lines of elements, or a continuum spectrum, was set up at the far end of a vacuum pipe ∼526 m from the HRMA. The purpose of the distance was so the beam would simulate a point source at infinity, although the actual source size of ~ 0.2 arcsec and beam divergence of ~ 4 arcmin need to be taken into account. These X-rays illuminate the HRMA, and also shine on beam normalization detectors (BND) placed at two stations. The building 500 location contained a flow proportional counter (FPC) and a Ge solid state detector (SSD), while four FPC were arranged just outside the entrance to the HRMA. The HRMA focussed X-rays through an array of pinhole apertures (not shown) which could be positioned in the focal plane, and onto FPC and SSD which were nominally identical to those used in the BND assemblies.

Our basic calibration principle was to determine the flux, F(E), of X-rays of energy E from the source by the counting rate R_{BND}(E) in the BND according to $\mathrm{F(E)} = \mathrm{R}_{BND}\mathrm{(E)}/(\mathrm{A}_{BND}\ \mathrm{Q}_{BND})$, where A_{BND} is the area of the BND. We would then use Eq. (1) where the response function of the focal plane detector Q_i was taken to be nominally identical to that of the BND, so that we could immediately cancel the response functions Q and derive the desired effective area

$$A(E) = (R_i(E)/R_{BND}(E)) \times A_{BND}. \tag{2}$$

This shows how the HRMA effective area is related to an absolute standard, via the chain of measurement by which we determine the area of the mechanical apertures on the BND. This technique makes the calibration virtually insensitive to time variations in the X-ray generator. Rather than using Eq. (2) exactly as above, the actual calculation also accounts for the different distances along the vacuum pipe, deadtime effects in detectors, whether the beam measured outside the HRMA footprint is uniform and identical to the intensity illuminating the HRMA, the extraction of the line flux at energy E or of the continuum flux in a finite energy channel, and all the higher order effects due to inevitable small differences in each individual detector.

Figure 2[3,5] illustrates the process. In this case a continuum spectrum was produced by bremsstrahlung on a carbon anode. The middle panel shows the derived counting rate spectrum in the building 500 BND SSD, while the top panel is the derived spectrum which was focussed by the mirror and passed through a 40 arcsec (2 mm)

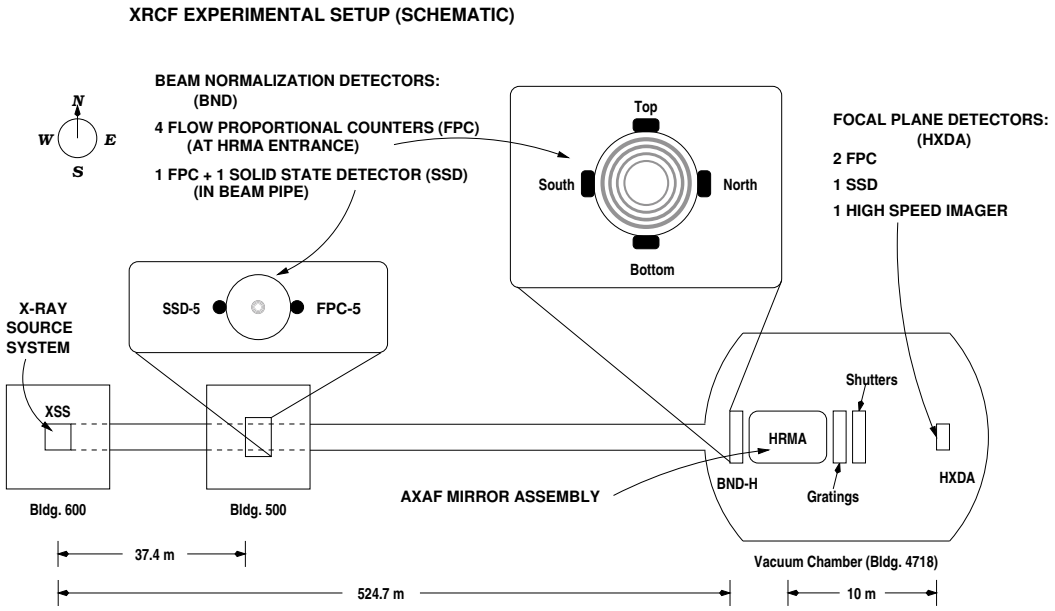

Figure 1. Configuration for the MSFC/XRCF HRMA calibration.

diameter aperture. The carbon target had impurities which we see as the characteristic X-ray lines indicated by the vertical dashed lines. Note the decreased counting rate at higher energies in the top panel, due to the critical grazing angle at those energies being smaller than the 41.3′ angle for shell 3 above about 5 keV. The ratio of top to middle panel, times the area of the BND aperture and corrected for the distance from the BND to the HRMA, gives the desired effective area. This is the primary data for the HRMA area calibration in the 2.2 to 10 keV range. At lower energies, the effects of ice condensing on the SSD begins to cause noticeable absorption which cannot be independently corrected, and the area data rely solely on measurements of characteristic X-ray lines.

3. SYNCHROTRON MEASUREMENT OF OPTICAL CONSTANTS

Direct ground calibration is not sufficient to give us the necessary information to the desired accuracy. We have already seen that during XRCF calibration incident X-rays which are nominally on-axis strike the HRMA at angles systematically different from those on-orbit by up to 4 arcmin. The calibration energies available at the XRCF are only the finite set produced as characteristic X-ray lines, or else the SSD continuum measurements which are effectively averaged over the $\sim$ 300 eV energy resolution bandwidth of the detector. Also, we need to know the area, and other mirror properties, at any arbitrary off-axis angle in the usable field of view. Our solution was to use the HRMA performance model described in Sect. 4, validated by a grid of XRCF measurements at a discrete set of energies and off-axis angles.

A critical input to this model is the reflection probability for an X-ray photon of energy E striking the mirror at a grazing angle α. For a perfectly smooth surface, this probability is the well-known Fresnel reflection coefficient. At a fixed angle, the Fresnel reflectivity uses the complex index of refraction $n = 1 - \delta - i\,\beta$, given by the optical constants (δ,β) as a function of energy. These constants are the product of intrinsic atomic scattering properties of the Ir, multiplied by the density.

We have performed measurements[6] to determine the Ir optical constants from 0.050 to 12 keV. These have involved synchrotron measurements of reflectivity at the Brookhaven National Laboratory[7] and at the Lawrence Berkeley Laboratory Advanced Light Source.[8] The measurements used witness flats prepared during the same series of coating runs in which the individual HRMA zerodur elements were sputtered with Cr and Ir.

We have used the NKFIT algorithm due to Windt[9] to derive optical constants in narrow energy bands (typically $E/\Delta E > 1000$), from reflectivity measurements at, typically, 6 to 8 different grazing angles. For grazing angles of interest in the energy region above $\sim$ 100 eV we may neglect the small difference in the parallel and perpendicular

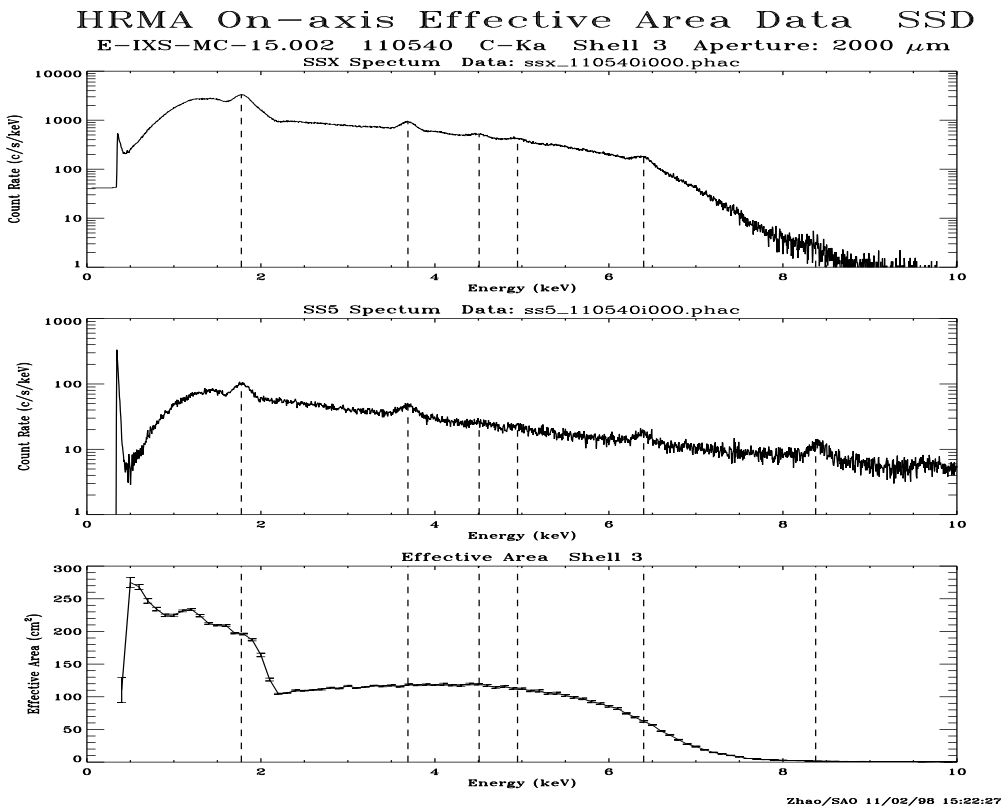

Figure 2. Measurement of the shell 3 area using the carbon-continuum source. Top panel shows the flux measured in the focal plane with the SSD. The middle panel shows the flux monitored by the BND. The ratio of the top two panels is the essential input to the effective mirror area shown in the bottom panel.

polarization components. The code can calculate the reflectivity from a multilayer array by applying the Fresnel coefficients for reflection and refraction at each interface.

We must also account for the scattering at each interface, due to the fact that the surfaces are not perfectly smooth. As an *approximation* we apply[10] a form of the Nevot-Croce factor[11]:

$$\exp -(2k_1 \cos\theta_1 \, k_2 \cos\theta_2 \, \sigma_{12}^2), \tag{3}$$

where the wavenumber $k_i = 2\pi \, n_i/\lambda$, with n_i the complex index of refraction in medium i, θ_1 the incident angle from the surface normal ($\theta = \pi - \alpha$) and θ_2 the angle of refraction. This formulation applies to the case where the correlation length of roughness along the interface is much smaller than the projected wavelength $\lambda/\cos\theta$. In the approximation, the parameter σ is regarded (cf. Ref.[12]) as the root-sum-squares of the classical surface microroughness amplitude and the variance of the Gaussian assumed to describe the density profile between one pure layer and another. We allow σ to be a free parameter of the fit.

Our initial analysis used a model with an infinite layer of zerodur, with finite layers of chromium and iridium, and with X-rays incident on the iridium from a vacuum. The thicknesses of the chromium and iridium layers were determined by the best fits to the reflectivity measured when scanning the grazing angle of the incident X-rays at fixed energy and observing the interference fringes in the region of low reflectivity. These were then fixed for the determination of the Ir optical constants. We use tabulated optical constants[13] for all elements other than Ir. This method gave extremely consistent values for the factor $\delta \equiv Re(n) - 1$ among all the different samples.[10] It is δ which is most significant for the reflection probability below the critical grazing angle.

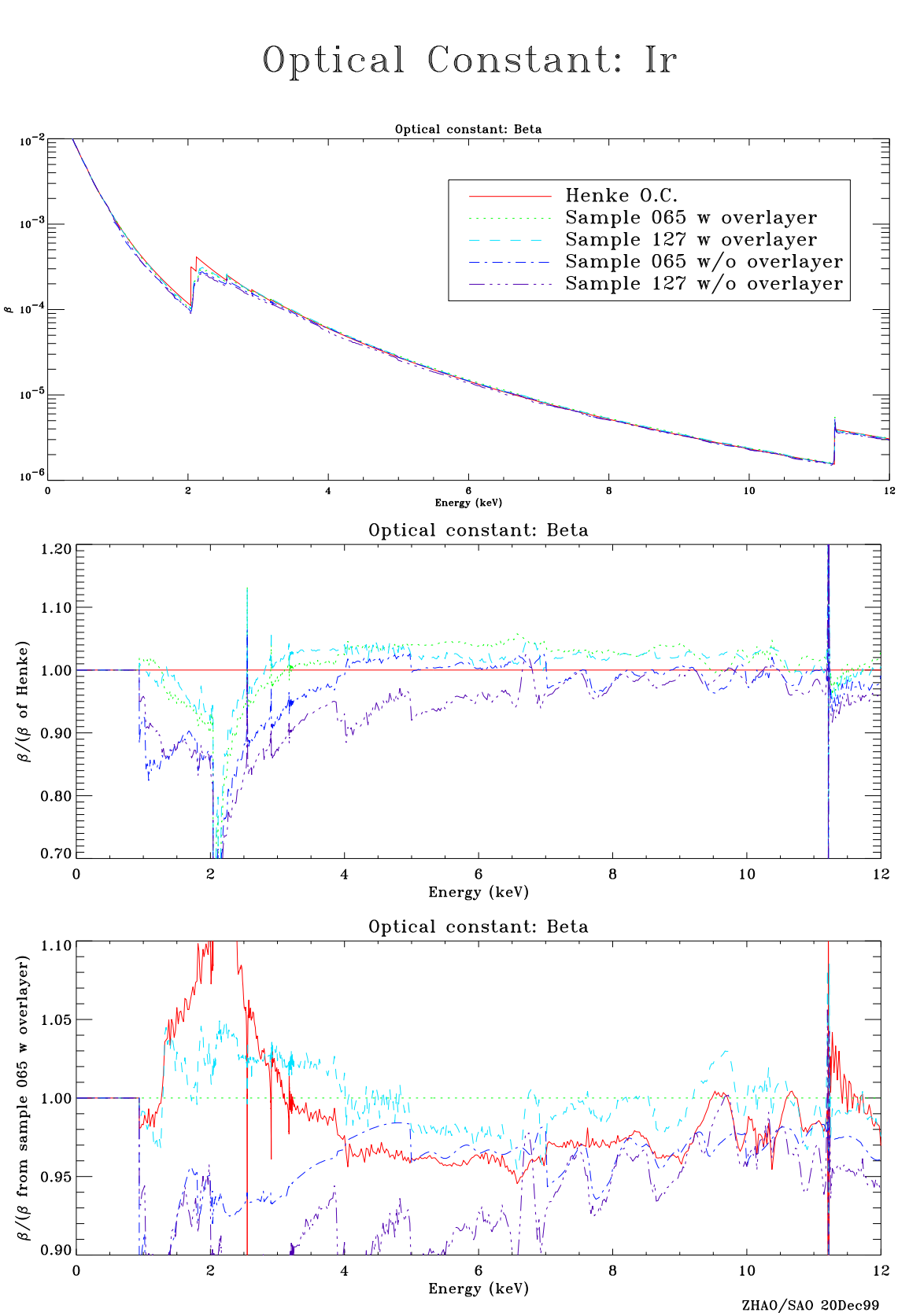

Figure 3. Synchrotron measurement of the optical constants β, showing improved agreement between samples when an overlayer is taken into account.

However, we noted[10] that the derived values of β, which is related to the mass absorption coefficient and which influences the reflectivity above the critical grazing angle, were correlated to the differing microroughness of the various optical witness samples used. This situation has been improved by realizing that an overlayer of molecular contamination would be expected. For analysis above 1 keV, we treat this layer simply as pure carbon with a variable thickness.

Figure 3 shows the resulting β. The top frame shows two of the witness samples, analyzed with and without the overlayer, and compared to the tabulated Henke constants[13] for Ir. The differences are from a few up to ten percent, except near the M-edges around 2.06 to 3.5 keV and L- edge at 11.2 keV, as shown by the ratios in the middle frame. The two samples analyzed with an overlayer, the dotted and the dashed lines in Fig. 3, give β values much closer to each other than are the same two data sets analyzed without the overlayer, and shown as the dot-dash and triple-dot dash lines. These are emphasized in the bottom panel where we take the ratio to the β for sample 065, with the overlayer.

Our philosophy in this analysis has been to produce optical constants which match the ground calibration data, and then use them to make on-orbit predictions. We recognize we are dealing with approximations for the interactions at the interfaces, for the unknown chemical composition of the hypothetical overlayer, and, possibly, with relative systematic errors in the synchrotron data sets. The latter are derived from several different setups of the beam line, each used over a factor of only 1.5 to 2.5 in energy in order to produce a beam with appropriate intensity and at the required angles, in the given energy range. We therefore allow some variation of the "uninteresting" parameters[14,15] in order to get a better match to the reflectivity data. While these variations of the layer thicknesses and roughness parameters are not physical, they are small (few Å), and we obtain good agreement of the optical constants in the regions of overlap. In fact, the thickness of the overlayer is surprisingly small, being fit typically with 9 to 13 Å. While we took great care to keep them dust-free, as was the HRMA, we did expose them to laboratory environments briefly and were not able to provide the same dry nitrogen purge which the HRMA had.

4. HRMA RAYTRACE MODEL

The original use of our raytrace model, based on the SAOsac raytrace suite[16] was to make performance predictions of the optical properties of the verification engineering test article[17] and to support the HRMA development. For this we originally considered only the Fresnel reflection from a single layer of iridium for the total reflection probability, with an angular distribution of scattered radiation predicted by a scalar scattering theory. To use the optical constants resulting from our synchrotron reflectivity measurements, we needed to apply the same reflectivity theory used in their derivation. Currently the SAOsac routines incorporate multilayer capability, and use the Nevot-Croce factor, Eq. 3, to multiply the Fresnel coefficient.

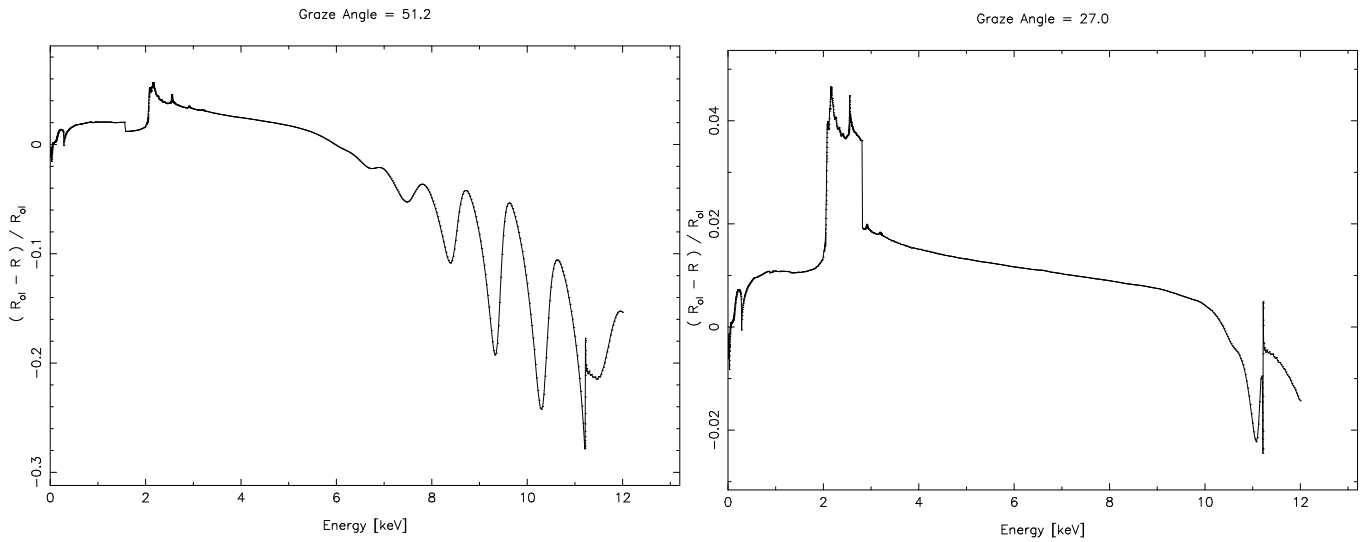

Figure 4. Modification of reflectivity by a 12 Å carbon overlayer.

One notable difference is that we do not utilize a contaminating overlayer, as was needed in our analysis of the synchrotron reflectivity data. We have no independent estimate of what the composition or thickness of such a layer would be. As efforts were made to prevent non-volatile condensates from contaminating the HRMA, we might expect less effect that on the synchrotron witness flats. Figure 4 shows the percentage effect that a 12 Å overlayer would have on the reflectivity of shell 1, left panel, and shell 6, right panel. The effect on the area would be twice the amount shown, since each X-ray undergoes two reflections to reach the focal plane. Such an overlayer would increase the area by about 2% at most energies, and about 8% in the Ir M-edge region. Note that shells 1 and 6 have virtually no area above 5 and 10 keV, respectively, so the large deviations and the oscillations due to interference fringes are of no consequence.

5. COMPARISON TO XRCF DATA

Figure 5 compares the best raytrace prediction of the HRMA performance at the XRCF, with the actual data which was obtained. For each shell, the upper figure of the pair shows the effective area in cm^2 measured by the SSD with the carbon target bremsstrahlung continuum (dotted line), measured by the FPC for discrete characteristic X-ray lines (diamonds) or predicted from the raytrace suite (solid line). The disagreement falls short of our accuracy goals; e.g., being up to 7% at 3 keV for shell 4 and at 9.5 keV for shell 6. However the agreement for the total HRMA, which is a more relevant quantity on-orbit, is within 4% everywhere up to 9.5 keV.

To force the model to agree with the data we apply an *ad hoc* correction factor.[3] For each shell, the lower panel gives the ratio of the data to the raytrace model. Above 2.2 keV this ratio is fitted to a 4th order polynomial for the SSD continuum region. Below 2 keV the average of the 2 or 3 discrete lines is taken as a constant correction factor. We believe this factor is needed due to the lack of an exact theory for scattering, which increasingly affects the reflectivity above the critical angle. Indeed, shell 1, which we measure to the highest energies above the critical angle and which also has the roughest surface as measured by Wyko interferometry, shows the greatest discrepancies.

This approach does not yet account for the discrete line measurements above 2 keV, show as the diamonds in Fig. 5. These are of comparable precision, but show different systematics, and give systematically about 5% less area that the SSD for the individual shells. However, when the areas of each shell is weighted by its contribution to the entire HRMA, the magnitude of this deviation is suppressed. Clearly, further analysis of the systematic errors is merited, and we intend to recompute the ground calibration correction factor by utilizing all the discrete line data as well as the continuum data.

6. ON-ORBIT EFFECTIVE AREA

To the extent that this correction factor is an intrinsic property of reflectivity, we believe it will apply identically to correct the on-axis performance as predicted by the raytrace. Figure 6 shows the predicted on-orbit area for the entire HRMA, solid line, as well as shell by shell. More specifically, this is the area, as a function of energy, which is effective in focussing a point source, *on-axis*, to within a 10 arcsec diameter circle. This will be a convenient "standard aperture" for precision photometry, as it is relatively insensitive to effects of the focal plane instruments' resolution or to imperfections in the aspect solution reconstruction. The HRMA effective area is actually computed by fitting its own polynomial correction factor to the XRCF data. This is nearly equal to the sum of the areas of the four shells, each determined with its own correction factor. However applying the correction factor to the HRMA as a whole results in a somewhat smoother fit, and uses fewer free parameters.

As we have said, there are no celestial X-ray standards which can be used to verify the mirror area to a precision of a few percent. One indirect check which can be made is to use the transmission gratings over an energy region which is so small that we may assume their efficiency and the detector efficiency vary by only a small amount. Figure 7[18] shows the response of the MEG and of the HEG to the continuum spectrum of the BL Lac object Mkn 421. The lower panel of each pair shows the raw counts per wavelength bin, plotted against wavelength in Å. At shorter wavelengths than 6.02 Å corresponding to the 2.06 keV Ir M-edge, we see a decrease in counting rate expected from Fig. 6. When this is corrected for the expected HRMA area, and for the grating transmission and the ACIS detector efficiency, the energy flux in the upper panel of each pair varies very smoothly[18] across the Ir M-edge, as expected for this class of object. The number of counts are not large, and the analysis is only preliminary, but we can probably place a conservative upper limit of no more than a 10% multiplicative error, or a 40 cm^2 additive error, to the change in HRMA area across this energy region.

Figure 8 shows the dependence of the effective area on the focal plane region which is used to define the events of interest. The 10 arcsec diameter region collects more than 90% of the photons at all energies, and thus has a relatively small correction from the measured numbers to the absolute photometry, defined as the total flux per cm^2 which is incident on the mirror and reflected into the entire 2π region of the focal plane. The 2 and 35 mm diameter apertures correspond to 40 arcsec and 11.67 arcmin diameters respectively. These were standard apertures used in the XRCF calibration, with the latter being larger than the flight imagers and used as the transfer standard to 2π coverage.

Calibration accuracy of the HRMA currently exceeds the demands imposed by current uncertainties in the focal plane instrument performance. If we consider the error made by the best raytrace prediction of the XRCF performance, we would estimate a 4% absolute uncertainty. If we believe that this error is due to the intrinsic physics of the reflection process, then our ad hoc correction should be valid for the on-orbit data, and our overall HRMA effective area would be known to better than 2%.

ACKNOWLEDGMENTS

Design, construction, alignment, and calibration of the Chandra HRMA is based on the work of hundreds of people. We thank the many technical and support personnel from NASA, SAO, MIT, PSU, LMA, TRW, EKC, HDOS, OCLI, SRON, and MPE who have contributed. This work was supported, in part, by NASA contracts NAS8-40224 and NAS8-39073, NASA grant NAG8-792, and SAO contract SV1-61010.

REFERENCES

1. M. C. Weisskopf, H. D. Tananbaum, L. P. VanSpeybroeck, and S. L. O'Dell, "Chandra X-ray Observatory: overview," in *X-Ray Optics, Instruments, and Missions*, J. Truemper and B. Aschenbach, eds., *Proc. SPIE* **4012**, 2000.
2. D. Jerius, R. J. Edgar, T. J. Gaetz, B. R. McNamara, D. A. Schwartz, L. P. VanSpeybroeck, and P. Zhao, "Orbital measurement and verification of the Chandra X-ray Observatory's PSF," in *X-Ray Optics, Instruments, and Missions*, J. Truemper and B. Aschenbach, eds., *Proc. SPIE* **4012**, 2000.
3. P. Zhao, "AXAF-mirror effective area calibration using the C-continuum source and solid state detectors," in *X-Ray Optics, Instruments, and Missions*, R. B. Hoover and A. B. C. Walker, Jr., eds., *Proc. SPIE* **3444**, pp. 234–257, 1998.
4. S. L. O'Dell and M. C. Weisskopf, "Advanced X-ray Astrophysics Facility (AXAF): Calibration overview," in *X-Ray Optics, Instruments, and Missions*, R. B. Hoover and A. B. C. Walker, Jr., eds., *Proc. SPIE* **3444**, pp. 2–18, 1998.
5. D. Jerius, ed., *XRCF Phase 1 Testing: Analysis Results*, http://hea-www.harvard.edu/MST/simul/xrcf/report/, Harvard-Smithsonian Center for Astrophysics, 1999.
6. D. E. Graessle, T. H. Burbine, J. C. Cobuzzi, E. M. Kellogg, D. A. Schwartz, R. L. Blake, and P. P. Gong, "Reflectance calibrations of axaf-mirror samples at absorption edges using synchrotron radiation," in *Multilayer and Grazing Incidence X-Ray/EUV Optics for Astronomy and Projection Lithography*, R. B. Hoover and A. B. C. Walker, Jr., eds., *Proc. SPIE* **1742**, pp. 203–218, 1992.
7. J. J. Fitch, R. L. Blake, A. J. Burek, A. M. Clark, D. E. Graessle, B. Harris, D. A. Schwartz, and J. Sweeney, "AXAF synchrotron witness mirror calibrations 2 to 12 keV," in *Grazing Incidence and Multilayer X-Ray Optical Systems*, R. B. Hoover and A. B. C. Walker, Jr., eds., *Proc. SPIE* **3113**, pp. 30–39, 1997.
8. B. Harris, A. J. Burek, J. J. Fitch, D. E. Graessle, D. A. Schwartz, R. L. Blake, and E. M. Gullikson, "Determination of optical constants for AXAF mirrors from 0.05 to 1.0 kev through reflectance measurements," in *Grazing Incidence and Multilayer X-Ray Optical Systems*, R. B. Hoover and A. B. C. Walker, Jr., eds., *Proc. SPIE* **3113**, pp. 40–51, 1997.
9. D. L. Windt, W. C. Cash, M. Scott, P. Arendt, B. Newman, R. F. Fisher, and A. B. Swartzlander, "Optical constants for thin films of C, diamond, Al, Si, and CVD SiC from 24 å to 1216 å," *Applied Optics* **27**, pp. 279–295, 1988.
10. D. E. Graessle, R. L. Blake, A. J. Burek, S. E. Dyson, J. J. Fitch, D. A. Schwartz, and R. Soufli, "Modeling of synchrotron reflectance calibrations of AXAF iridium-coated witness mirrors over 2 to 12 kev," in *X-Ray Optics, Instruments, and Missions*, R. B. Hoover and A. B. C. Walker, Jr., eds., *Proc. SPIE* **3444**, pp. 140–159, 1998.

11. L. Nevot and P. Croce, "Caracterisation des surfaces par reflexion rasante de rayons X. application a l'etude du polissage de quelques verres silicates," *Rev. Phys. Appl.* **15**, pp. 761–779, 1980.
12. D. K. G. de Boer, "X-ray scattering and x-ray fluorescence from materials with rough interfaces," *Phys. Rev. B* **53**, pp. 6048–6064, 1996.
13. B. L. Henke, E. M. Gullikson, and J. C. Davis, "X-ray interactions: photoabsorption, scattering, transmission, and reflection at E=50-30,000 eV, Z=1-92," *Atomic Data and Nuclear Data Tables* **54**, pp. 181–342, 1993.
14. Y. Avni, "Energy spectra of x-ray clusters of galaxies," *Astrophysical Journal* **210**, pp. 642–646, 1976.
15. M. Lampton, B. Margon, and S. Bowyer, "Parameter estimation in x-ray astronomy," *Astrophysical Journal* **208**, pp. 177–190, 1976.
16. J. P. Hughes, D. A. Schwartz, A. H. Szentgyorgyi, L. P. VanSpeybroeck, and P. Zhao, "Surface finish quality of the outer AXAF mirror pair based on x-ray measurements of the VETA-I," in *Multilayer and Grazing Incidence X-Ray/EUV Optics for Astronomy and Projection Lithography*, R. B. Hoover and A. B. C. Walker, Jr., eds., *Proc. SPIE* **1742**, pp. 152–161, 1992.
17. M. C. Weisskopf, "AXAF VETA test: an overview," in *Multilayer and Grazing Incidence X-Ray/EUV Optics for Astronomy and Projection Lithography*, R. B. Hoover and A. B. C. Walker, Jr., eds., *Proc. SPIE* **1742**, pp. 2–5, 1992.
18. H. L. Marshall, "High resolution x-ray imaging and spectroscopy of AGN and SS 433 with the Chandra X-ray Observatory," in *Astrophysical Phenomena Revealed by Space VLBI*, H. Hirabayashi, P. G. Edwards, and D. W. Murphy, eds., p. in press, 2000.

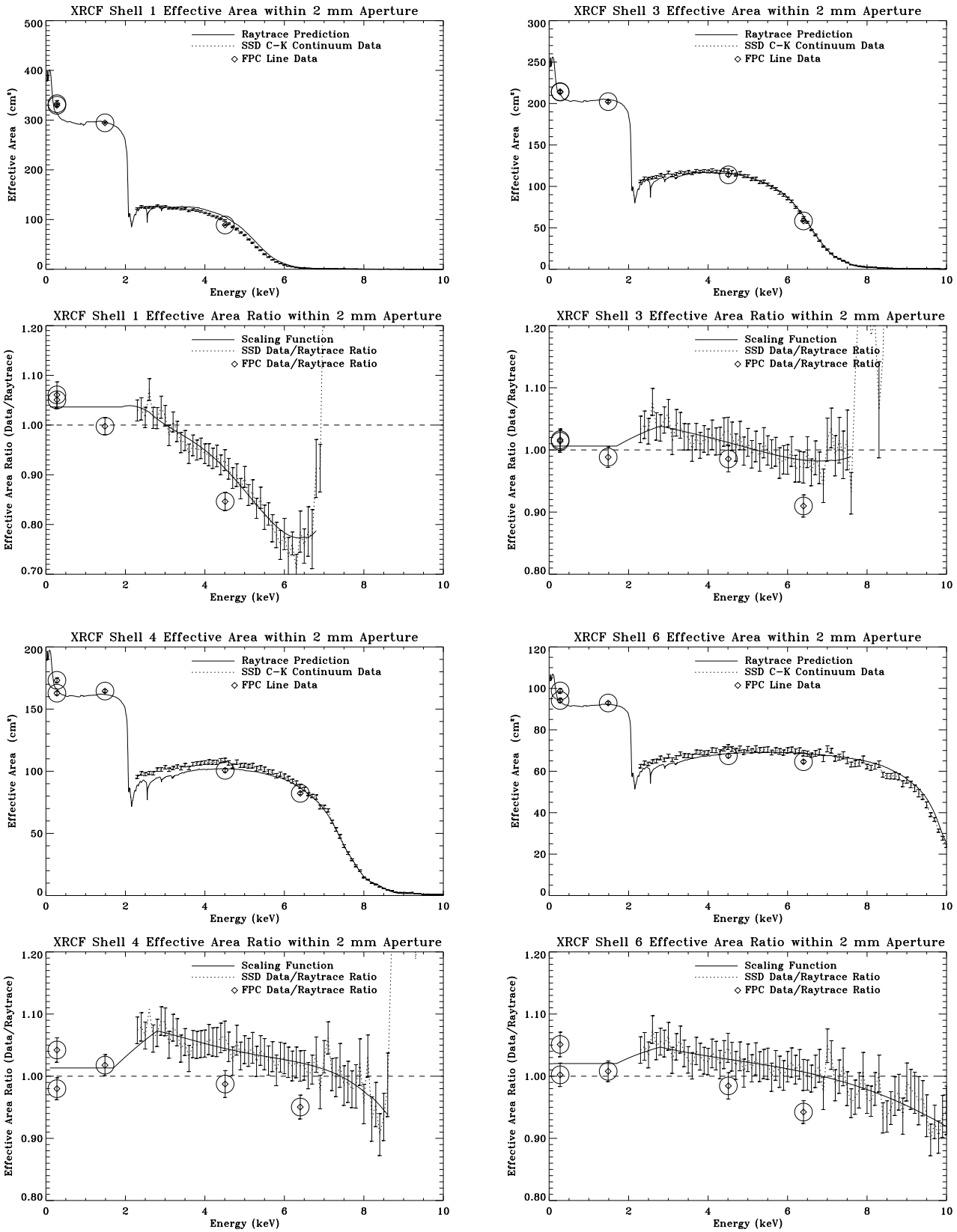

Figure 5. Shell by shell comparison of the final raytrace predictions, solid lines in the upper panel of each pair, to the effective area measured at the XRCF. Dotted lines through the data points give the effective area measured by the SSD, with the bremsstrahlung continuum from the carbon target. The diamonds give the area measured by the FPC, using characteristic X-ray lines. The lower panel of each pair gives the ratio of the XRCF results to the raytrace prediction, and the solid line in those figures shows the ad hoc correction factor we adopt.

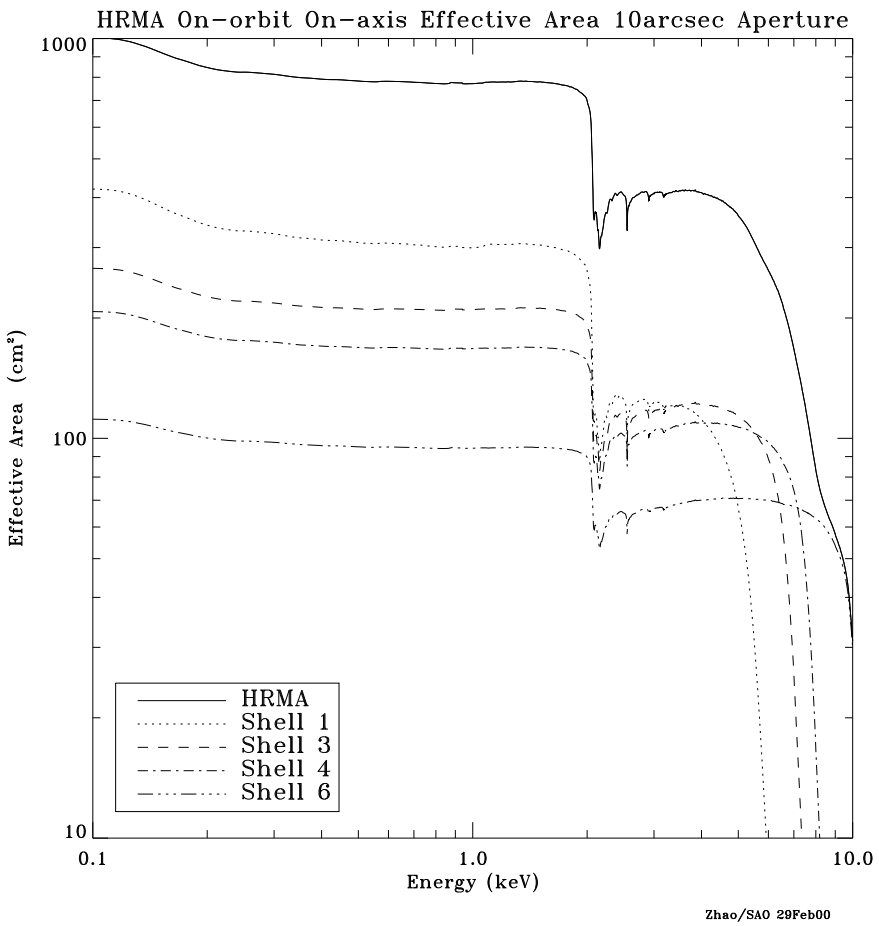

Figure 6. Estimate of the effective on-axis area on-orbit, for photons collected in a 10 arcsec diameter circle.

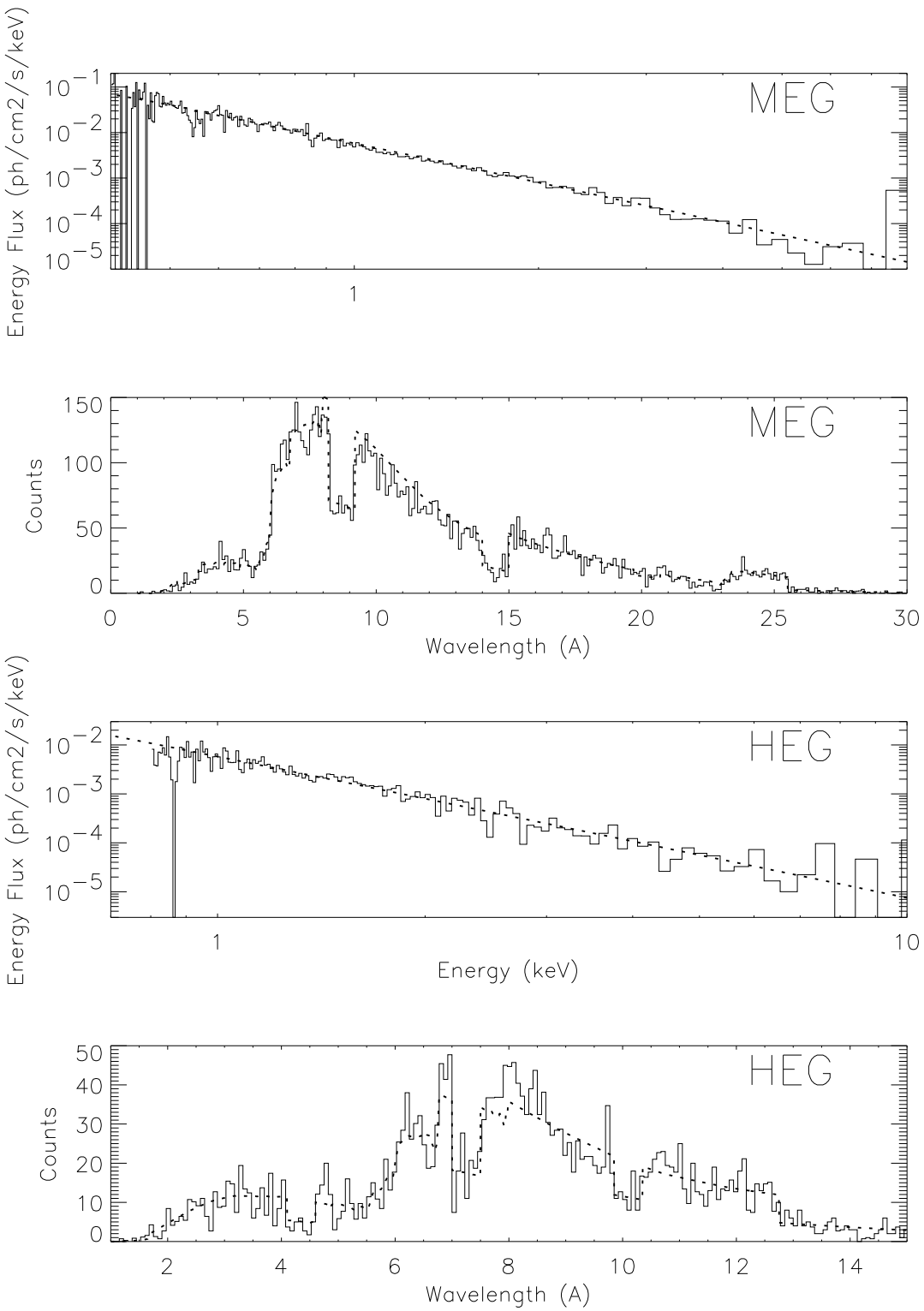

Figure 7. HETG measurement of the spectrum of Mkn 421.[18] The flattening of the raw data by the correction for the HRMA effective area shows that the latter is correct to within 10% across the Ir M-edges.

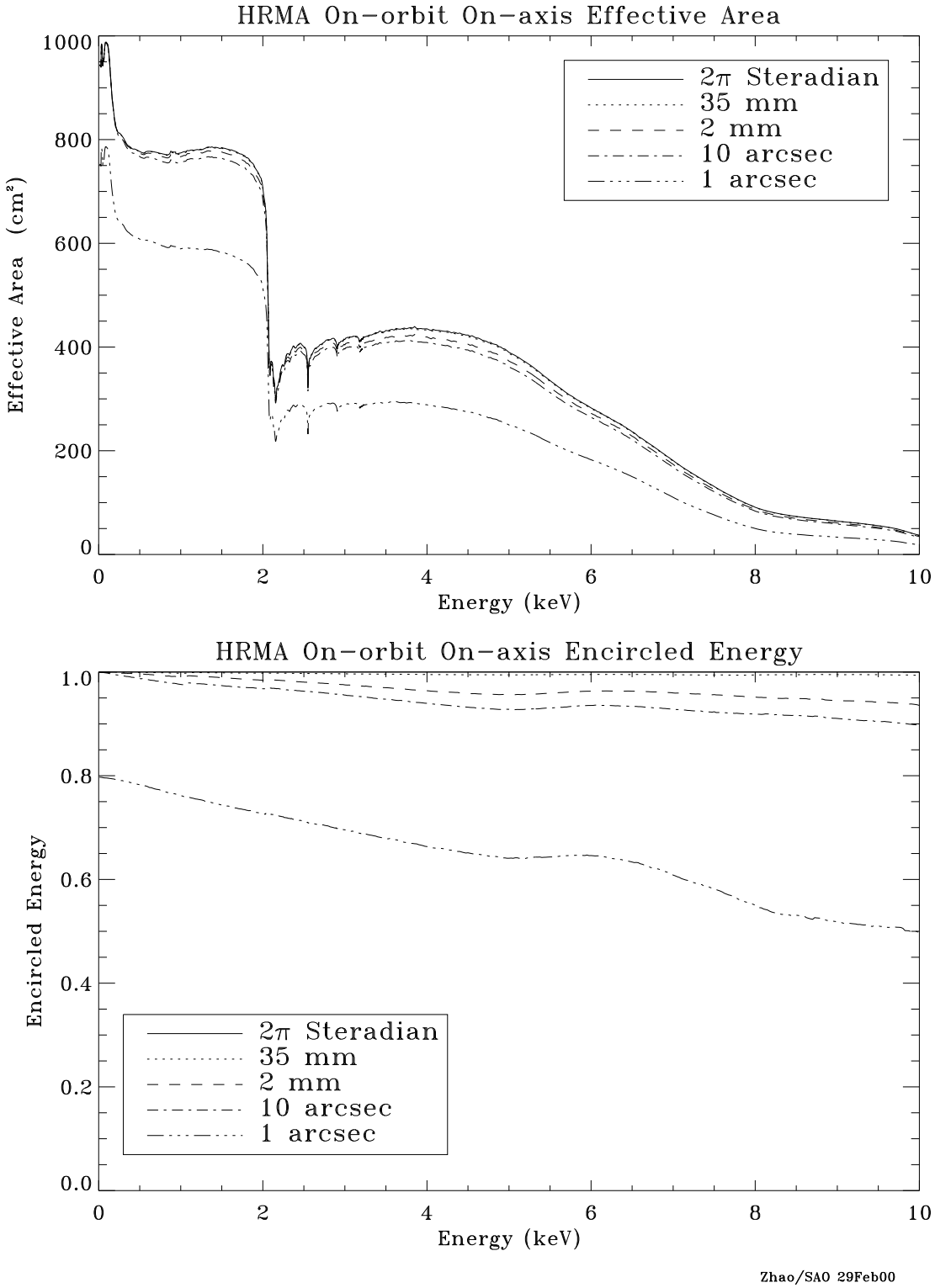

Figure 8. Scaling of the effective area on-orbit according to the effective aperture used to collect photons. The top figure is a linear plot of the effective area, and the bottom figure shows the fraction in given apertures as a ratio to the total collecting area for photons reaching an abitrary region of the focal plane.